Chemical Promenades: Exploring Potential-energy Surfaces with Immersive Virtual Reality

Marta Martino,[a†] Andrea Salvadori,[a†] Federico Lazzari,[a] Lorenzo Paoloni,[a] Surajit Nandi,[a] Giordano Mancini,[a] Vincenzo Barone[a] and Sergio Rampino[a*]

March 6, 2020

Abstract

The virtual-reality framework AVATAR (Advanced Virtual Approach to Topological Analysis of Reactivity) for the immersive exploration of potential-energy landscapes is presented. AVATAR is based on modern consumer-grade virtual-reality technology and builds on two key concepts: 1) the reduction of the dimensionality of the potential-energy surface to two process-tailored, physically meaningful generalized coordinates, and 2) the analogy between the evolution of a chemical process and a pathway through valleys (potential wells) and mountain passes (saddle points) of the associated potential energy landscape. Examples including the discovery of competitive reaction paths in simple A + BC collisional systems and the interconversion between conformers in ring-puckering motions of flexible rings highlight the innovation potential that augmented and virtual reality convey for teaching, training and supporting research in chemistry.

Keywords: Potential energy surface, Immersive virtual reality, Atom diatom reactions, Ring puckering motions.

[a]SMART Laboratory, Scuola Normale Superiore, Piazza dei Cavalieri 7, 56126 Pisa, Italy

[†]M. Martino and A. Salvadori contributed equally to this work.

[*]Correspondence to: S. Rampino (sergio.rampino@sns.it).

A researcher tracking the evolution of the C + CH^+ $\rightarrow$ C_2^+ + H reaction by immersive exploration of valleys (potential wells) and mountain passes (saddle points) of the associated potential energy landscape.

1 INTRODUCTION

As well known, rigorous simulations of molecular processes should be based on the solution of the Schrödinger equation for the wavefunction of the involved nuclei and electrons, which is usually cast in its non-relativistic time-independent form with a Hamiltonian including a kinetic term for the electrons $\hat{T}_e$, a kinetic term for the nuclei $\hat{T}_N$, and an interaction-potential term $V(\mathbf{r},\mathbf{R})$, with $\mathbf{r}$ and $\mathbf{R}$ being the set of spatial coordinates of electrons and nuclei, respectively. This equation is seldom solved as is, due to the associated mathematical difficulties and computational cost. More commonly, on the grounds that the nuclei are much heavier than the electrons, the Born-Oppenheimer approximation[1] is adopted and the problem is broken down in two separate problems, one for the motion of the electrons at a given nuclear geometry:

$$\left[\hat{T}_e + V(\mathbf{r};\mathbf{R})\right] \varphi_n(\mathbf{r};\mathbf{R}) = \varepsilon_n(\mathbf{R})\varphi_n(\mathbf{r};\mathbf{R}) \; , \tag{1}$$

and one for the motion of the nuclei under the action of a potential term $\varepsilon_n(\mathbf{R})$ associated with electronic state n:

$$\left[\hat{T}_N + \varepsilon_n(\mathbf{R})\right] \Phi_n(\mathbf{R}) = E_n \Phi_n(\mathbf{R}) \; . \tag{2}$$

The collection of the values of $\varepsilon_n(\mathbf{R})$ for all possible nuclear geometries is the so-called potential-energy surface (PES), which represents a well-known key concept and plays a central role in many facets of chemistry such as reaction diagrams, thermodynamics, spectroscopy, and in governing the dynamics and kinetics of chemical processes.

The PES $\varepsilon_n(\mathbf{R})$ of an N-atom molecular system is an inherently multi-dimensional function, or hypersurface, depending on the related $3N-6$ generalized coordinates. Such complexity is usually over-simplified by reducing the PES to a number of 'connected' stationary points making up a one-dimensional diagram accounting for most of the involved chemistry. On the other hand, modeling and interpreting spectroscopic and dynamical features of a molecular system requires the analysis of the PES as a function of at least a few degrees of freedom, typically those which are mostly involved in the physical process of interest[2–6]. A useful approach in this respect is that of opportunely reducing the dimensionality of the PES to two coordinates and build a three-dimensional representation where the selected

coordinates are used as the latitude and the longitude and the associated value of the PES as the elevation. The resulting representation has been conveniently used over the past few decades (see many of the references cited later on in this work) for studying the PES through contour plots analogous to those used for representing reliefs in geographic maps.

Nowadays the advent of immersive-virtual-reality (IVR) technology is revolutionizing the way of conceiving and exploiting scientific visualization. IVR technology offers in fact the unprecedented possibility of immersing oneself in three-dimensional representations of scientific data, where exploration and analysis are enhanced by one's own perceptive and proprioceptive system and by additional information displayed in an augmented-reality fashion. Based on state-of-the-art IVR technology, we have developed a virtual laboratory for the analysis of intermolecular interactions[7,8] based on a recently devised technique capable of disentangling and quantifying chemically-meaningful bonding components[9–12]. Leveraging on our experience in the development of such virtual laboratory, and motivated by the interest witnessed by recent works by Reihers' and Glowacki's groups on PES exploration through haptic devices[13–15] or real-time molecular dynamics simulations[16], we have developed AVATAR (Advanced Virtual Approach to Topological Analysis of Reactivity), an IVR application based on head-mounted displays and handheld controllers that takes advantage of IVR for the specific task of immersive visual analysis of potential-energy surfaces based on the following two key concepts: 1) the reduction of the dimensionality of the potential-energy surface to two process-tailored, physically meaningful generalized coordinates, and 2) the analogy between the evolution of a chemical process and a pathway through valleys (potential wells) and mountain passes (saddle points) of the associated potential energy landscape.

The outline of the article is as follows. In Section 2, we discuss process-tailored dimensionality-reduction schemes applied to two classes of problems: gas-phase prototype chemical reactions and ring-puckering motions of flexible rings. In Section 3, the AVATAR application is presented (see the Appendix for further technical details). In Section 4, we illustrate two case studies, namely the astrochemically relevant reaction C + CH^+ and the conformational analysis of silacyclopentane. In Section 5, conclusions are drawn and perspectives are outlined.

2 PES and dimensionality reduction

As mentioned above, the description of the relative assembly of an N-atom system is achieved by using $3N-6$ independent geometrical coordinates. In order to represent these potential energy surfaces in 3D IVR environments, this number has to be opportunely reduced to two dimensions (given the obvious limitation of human perception). In fact, unless a non geometric encoding is used for the energy, in a three-dimensional space there are only two dimensions available for describing the geometry of the system, since the third dimension has then to be used to represent the potential energy values. This creates a dichotomy because in a high dimension (hyper)surface the application of exhaustive sampling and search techniques is not straightforward and, as noted by Haag and Reiher,[15] being able to tap into chemical intuition would enhance the exploration. This also implies that, beside cited challenges shared with other scenarios of molecular visualization in IVR frameworks, PES visualization presents difficulties that are commonly encountered in multivariate data visualization. In this context, various techniques have been devised to (i) show the (whole) data set using different graphical paradigms[17] and (ii) reduce its dimensionality.[18] The second approach is particularly relevant in molecular modeling and it has also been often exploited, e.g. to perform calculations in systems composed by up to thousands of atoms[19,20]. In these studies, Principal Component Analysis (PCA), the most widespread of feature extraction techniques, is used to reduce the dimensionality of the problem. However, PCA based approaches suffer from many drawbacks, including their inability to capture any nonlinear nature of data and also to characterize strong overlapping data. To the best of our knowledge, the use of manifold learning techniques (such as t-SNE[21]) while common in other research fields (e.g. bioinformatics) is still limited in computational chemistry.

While all these techniques can be used in the pre-processing stage, a useful alternative approach is that of adopting specialized sets of *ad hoc* defined coordinates. In particular, the recipe that we exploit in AVATAR is as follows: 1) perform a change of coordinates by opportunely combining the generalized coordinates thus obtaining a new set of coordinates, two of which have a high descriptive value for the process under investigation (so-called 'process coordinates'); 2) for each combination of the values of these two coordinates, relax

the potential energy with respect to all other coordinates to get a so-called 'relaxed' 3D representation of the energy landscape as a function of the two process coordinates. The application of this scheme to two classes of processes is illustrated in the remainder of this section.

Atom-diatom reactions

The simplest chemical reaction where one bond is broken and a new one is formed is the gas-phase three-atom rearrangement process:

$$\mathrm{A} + \mathrm{BC} \rightarrow \mathrm{AB} + \mathrm{C}$$

Though the simplicity of such process makes it look a mere abstract model far from the complexity of the real world, this kind of reactive collisions can actually be experimentally reproduced and characterized through so-called crossed-molecular-beam experiments[22] and are of prominent relevance in astrochemistry due to the extreme conditions of low temperatures and pressure of the interstellar medium[23]. From a computational point of view, the modeling of these reactions typically requires the calculation of a set of electronic energies (usually those of the ground-state) at several nuclear geometries, the fitting or interpolation of these values to get a functional representation of the PES, and the use of this PES for the solution of the nuclear Schrödinger equation (Eq. 2).[24,25] A similar workflow has for instance been assembled, with contributions from one of the present authors, in the so-called Grid-Empowered Molecular Simulator GEMS[26,27] for execution on grid- and cloud- computing infrastructures and later on applied to several reactive processes such as N + N_2[28–30], O + O_2[31,32], and Li + FH[33].

As A + BC reactions involve 3 atoms ($N = 3$), the associated PES depends on $3N - 6 = 3$ generalized coordinates. A set of generalized coordinates commonly adopted for the description of the A + BC → AB + C process is that shown on top of Fig. 1, consisting of two internuclear distances (those of the breaking and forming bonds) and the angle between them. Useful two-dimensional PES representations may be obtained by retaining the two distances and either fixing the angle or minimizing the energy with respect to it. While these plots are widely adopted and provide a useful description of fixed-angle or minimum-energy

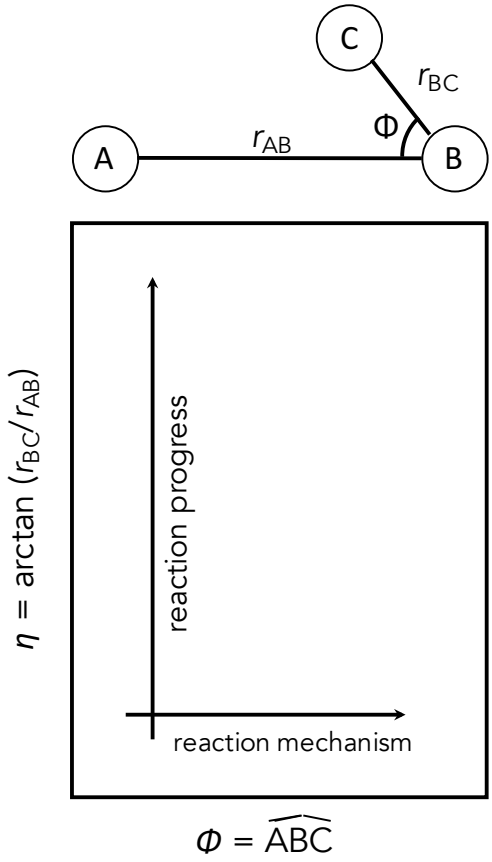

Figure 1: Rectangular relaxed plot of the PES for A + BC → AB + C reactions by means of the 'reaction-progress' and 'reaction-mechanism' coordinates η and Φ, respectively.

reaction paths, information on possible competing reaction mechanisms involving different atom-diatom approaching or scattering angles is undoubtedly lost.

A more informative representation is the so-called rectangular relaxed plot[31,32] where the PES for a given atom-diatom exchange reaction is represented as a function of a 'reaction-progress' and a 'reaction-mechanism' coordinate based on the following coordinate change:

$$\eta = \arctan(r_{\mathrm{BC}}/r_{\mathrm{AB}}) \tag{3}$$

$$\Phi = \widehat{ABC} \tag{4}$$

$$\rho = \sqrt{r_{\mathrm{AB}}^2 + r_{\mathrm{BC}}^2} \tag{5}$$

The first of these coordinates, η, is clearly a reaction-progress coordinate in that it measures the ratio between the breaking- over the forming-bond distance. The second coordinate accounts for the detailed mechanism by which the reaction occurs, as it relates to the approaching angle of A towards BC and the scattering angle of C from the newly formed AB diatom. The third coordinate is an 'overall-size' coordinate with less informative content.

A rectangular relaxed plot (see Fig. 1) is obtained by plotting for each couple (η, Φ) the value of the potential-energy minimized with respect to ρ, i.e.: $\min_{\rho} V(\eta, \Phi)$. The name rectangular derives from the shape of the domain of points usually adopted in such representation, where reaction progress is emphasized by using the long side of the rectangle for coordinate η and the short side for coordinate Φ. Moving along the horizontal axis of the rectangle in Fig. 1, the Φ angle changes providing information about the detailed mechanism of the reaction, while moving along the vertical axis the η angle changes quantifying the progress of the reaction. It is worth mentioning here that other useful alternatives exist for triatomic systems, based on different coordinate transformations such as triangular[34] and hyperspherical[35] ones.

Ring-puckering motions

Vibrational motions of molecules can be experimentally probed by several spectroscopic techniques such as infrared, vibrationally-resolved electronic and rotational spectroscopies, and significant efforts are devoted in our group to the accurate reproduction of vibrational and vibrationally resolved experimental spectra through computational methods[36–38]. In the context of conformational analysis of flexible cyclic molecules, a set of useful process coordinates for describing ring-puckering motions is that devised by Cremer and Pople[39], the so-called ring-puckering coordinates[40] (see also Ref. 41, where a clever way to describe in-plane deformations through ring-deformation coordinates is proposed). In this context an accurate representation of the PES as a function of these few coordinates is essential for modeling such large-amplitude motions by solving Eq. 2 in a reduced-dimensionality approach (semirigid model[42], also known as flexible model[43] or adiabatic-constraint approach[44]).

Cremer-Pople coordinates[39,45] allow for a complete description of ring-puckering motions in flexible-ring molecules with a set of $N_{\text{ring}} - 3$ coordinates, where N_{ring} is the number of

atoms belonging to the ring structure (e.g. in the case of the cyclopentane molecule only the five carbon atoms, therefore $N_{\mathrm{ring}} = 5$). After rotating and translating the Cartesian framework in which the coordinates of the molecular system under investigation are given according to the following prescriptions[39]:

$$\sum_{j=1}^{N_{\mathrm{ring}}} \mathbf{r}_j = 0 \tag{6}$$

$$\mathbf{r}' = \sum_{j=1}^{N_{\mathrm{ring}}} \mathbf{r}_j \sin\Big(\frac{2\pi(j-1)}{N_{\mathrm{ring}}}\Big) \tag{7}$$

$$\mathbf{r}'' = \sum_{j=1}^{N_{\mathrm{ring}}} \mathbf{r}_j \cos\Big(\frac{2\pi(j-1)}{N_{\mathrm{ring}}}\Big) \tag{8}$$

$$\hat{\mathbf{z}} = \frac{\mathbf{r}' \times \mathbf{r}''}{|\mathbf{r}' \times \mathbf{r}''|}\ , \tag{9}$$

where the position vectors $\mathbf{r}_j$ specify the positions of the atoms involved in the ring structure, the Cremer-Pople coordinates are defined as follows[40,45]:

$$\begin{aligned} q_m = \Big(\frac{2}{N_{\mathrm{ring}}}\Big)^{\frac{1}{2}} \Bigg\{ \Bigg[\sum_{j=1}^{N_{\mathrm{ring}}} z_j \cos\Big(\frac{2\pi m(j-1)}{N_{\mathrm{ring}}}\Big)\Bigg]^2 + \\ + \Bigg[\sum_{j=1}^{N_{\mathrm{ring}}} z_j \sin\Big(\frac{2\pi m(j-1)}{N_{\mathrm{ring}}}\Big)\Bigg]^2 \Bigg\}^{\frac{1}{2}} \end{aligned} \tag{10}$$

$$\theta_m = \begin{cases} \arctan\left[-\dfrac{\sum_{j=1}^{N_{\mathrm{ring}}} z_j \sin\left(\frac{2\pi m(j-1)}{N_{\mathrm{ring}}}\right)}{\sum_{j=1}^{N_{\mathrm{ring}}} z_j \cos\left(\frac{2\pi m(j-1)}{N_{\mathrm{ring}}}\right)}\right] & \text{if } \cos\theta_m > 0 \\ \arctan\left[-\dfrac{\sum_{j=1}^{N_{\mathrm{ring}}} z_j \sin\left(\frac{2\pi m(j-1)}{N_{\mathrm{ring}}}\right)}{\sum_{j=1}^{N_{\mathrm{ring}}} z_j \cos\left(\frac{2\pi m(j-1)}{N_{\mathrm{ring}}}\right)}\right] + \pi & \text{if } \cos\theta_m < 0 \\ \mathrm{sgn}[\sin(\theta_m)]\frac{\pi}{2} & \text{if } \cos\theta_m = 0 \end{cases} \tag{11}$$

If N_{ring} is even, m can assume values in the interval $2, ..., (N_{\mathrm{ring}} - 1)/2$, while $q_m > 0$ and $0 < \theta_m < 2\pi$. If N_{ring} is odd, $m = 2, ..., (N_{\mathrm{ring}} - 2)/2$ and another coordinate $q_{N/2}$ (which can assume both positive and negative values) is employed to describe the puckering amplitude of the crown form:

$$q_{N_{\mathrm{ring}}/2} = \Big(\frac{1}{N_{\mathrm{ring}}}\Big)^{\frac{1}{2}} \sum_{j=1}^{N_{\mathrm{ring}}} z_j \cos[(j-1)\pi]. \tag{12}$$

Accordingly, for a 5-term ring molecular system, ring-puckering motions can be described with only 2 coordinates: a puckering amplitude q and a pseudorotation angle θ. A reduced dimensionality PES suitable for analysis in an IVR environment can thus be obtained by plotting the energy as a function of the two polar coordinates q and θ (with $q > 0$ and $0 < \theta < 2\pi$) minimized with respect to all remaining coordinates. As detailed in Ref. 40, the value of the amplitude q measures the displacement from ring planarity while the meaning of the pseudorotation angle θ is better understood by inspection of the graphical representation (firstly proposed by Altona and Sundaralingam[46], and next used by other authors[47–49]) given in Figure 2, where twenty different conformations are shown for the corresponding twenty values of θ.

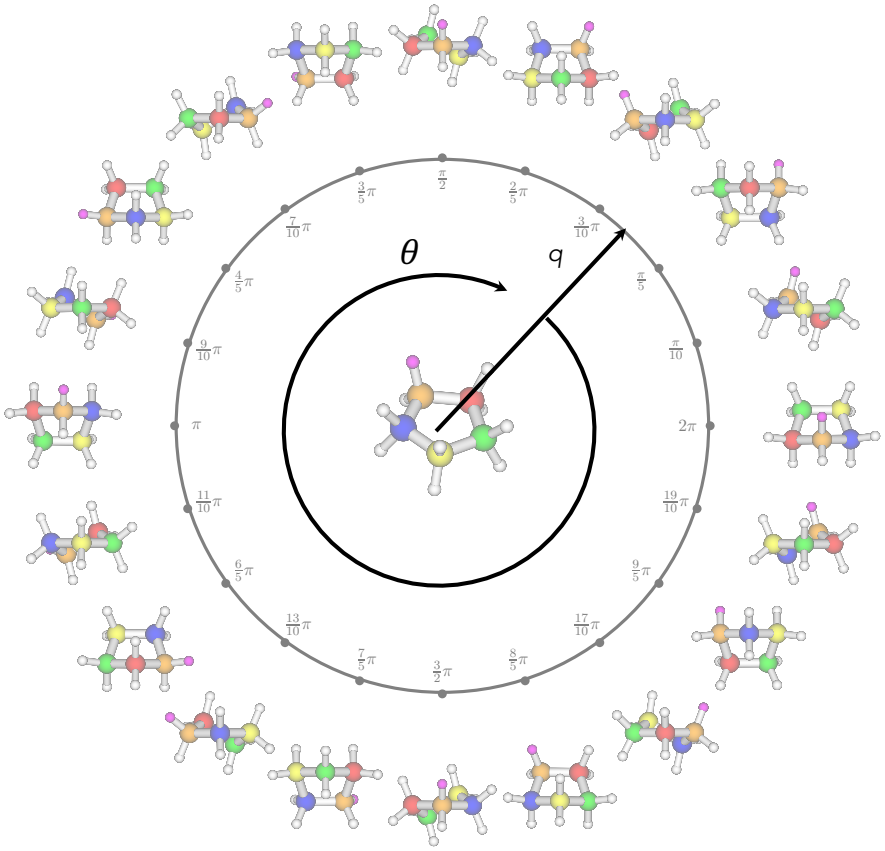

Figure 2: Circular relaxed plots of the PES for ring-puckering in 5-term rings by means of the puckering amplitude q and the pseudorotation angle θ.

3 AVATAR

AVATAR is a software for the immersive exploration of potential-energy landscapes specifically designed for the HTC Vive head-mounted display (HMD, https://www.vive.com) available at http://smart.sns.it/avatar. The program has been developed using the popular Unity game engine (https://unity3d.com/). This choice was made so as to take advantage of the out-of-the-box support for consumer-grade VR helmets provided by Unity, as well as of the massive amount of dedicated third-party software libraries and graphical assets (many of which are free and/or open source). Among the third-party libraries we used,[1] it is worth citing the VRTK (http://vrtk.io/) toolkit, which greatly simplifies the implementation of user interaction in virtual environments, and the Accord.Net framework[50] which provides a comprehensive set of procedures for linear algebra, geometry, statistics and machine learning.

The application is logically organized in two stages. The first stage concerns loading of the data and setting of various parameters related to the visualization of the PES. During this stage, the user interacts with the program by means of a standard desktop-based user interface. Then the immersive exploration takes place, in which the user wears the HTC Vive VR headset to walk around a virtual world having the PES as terrain.

Pre-processing

When launched, the AVATAR application shows a very simple start screen where the user can load a data file containing a regular sampling of a bidimensional PES. In order to foster the use of the program, we chose to adopt the simple and widespread "XYZ" file format (with minor additional prescriptions) as input of our program. In particular, AVATAR requires a multi-model XYZ file, where each model stores the atomic coordinates associated to a sample point of the energy surface. Furthermore, in each model, the comment line must contain the value of the related potential energy as well as the position of the sample point within the sampling grid. A detailed description of the input file format is provided in Appendix A.

Once the PES file has been loaded, a configuration panel is presented to the user, as

[1] The complete list of third-party software libraries and graphical assets employed in this project, accompanied by their respective copyright notices and licenses, will be made available with the software binaries.

shown in Fig. 3. Here the user can get a low-resolution preview of the color-mapped PES

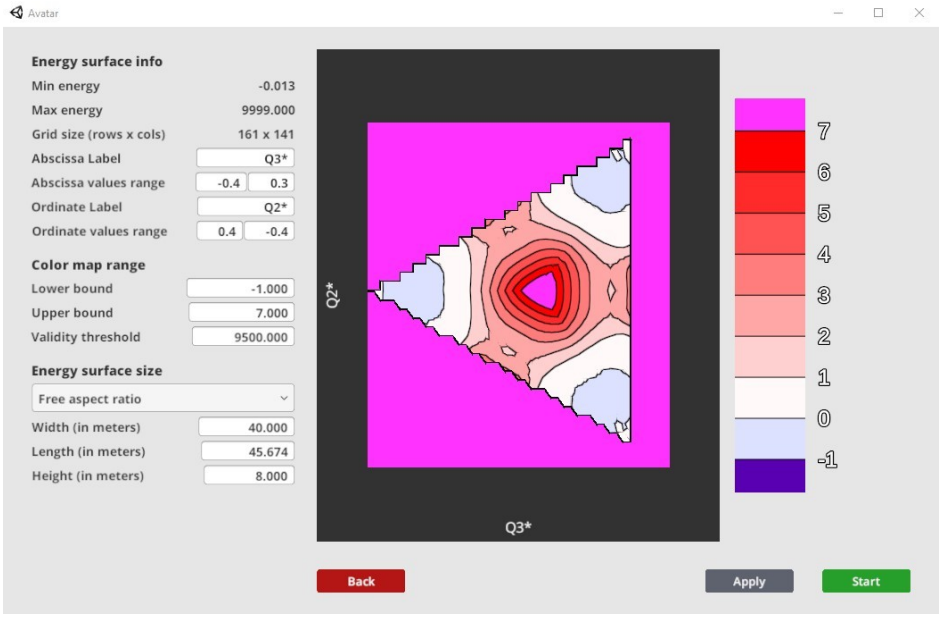

Figure 3: The configuration panel allows the user to set the range of values of the color map and the size of the PES in the virtual world. These settings are previewed on the left side of the panel. The example shown in this figure is a triangular[34] relaxed plot for reaction N + N_2.

and change several parameters related to the range of values of the color map as well as to the size of the PES in the virtual world. In particular, the form at the left-hand side of the panel is organized in three sections (see Fig. 3). The first section shows some general information about the sampled PES, such as the minimum and maximum energy values and the number of sample points along the two dimensions of the grid. The second section allows the user to specify the range of values to be represented by the color map and a "validity threshold" through which certain regions of the original rectangular domain can be excluded, as required for instance in circular plots such as those of Fig. 2. The original dataset is thus filtered in two ways: the color-map range is used to exclude, for instance, steep-gradient regions that arise from atoms approaching closely so that these do not hinder or obstruct the exploration, while the validity threshold is used to mark unphysical regions (further details on the validity threshold can be found in Appendix B). Finally, the third section of the configuration panel allows the user to set the size (width, length, and height)

of the PES in the virtual world. The user can get a preview of the new settings by means of the map located at the right-hand side of the configuration panel. When satisfied, the user presses the "Start" button and wears the VR helmet. The exploration of the energy surface in virtual reality can now begin.

Immersive session

The user finds himself immersed in a virtual world in which both the colors and the height of the terrain are functions of the energy values in the input-provided domain of points (see Fig. 4 showing the case of a rectangular relaxed representation of the C + CH^+ PES discussed later on in this article). We developed a dedicated shader[2] to color the surface according to

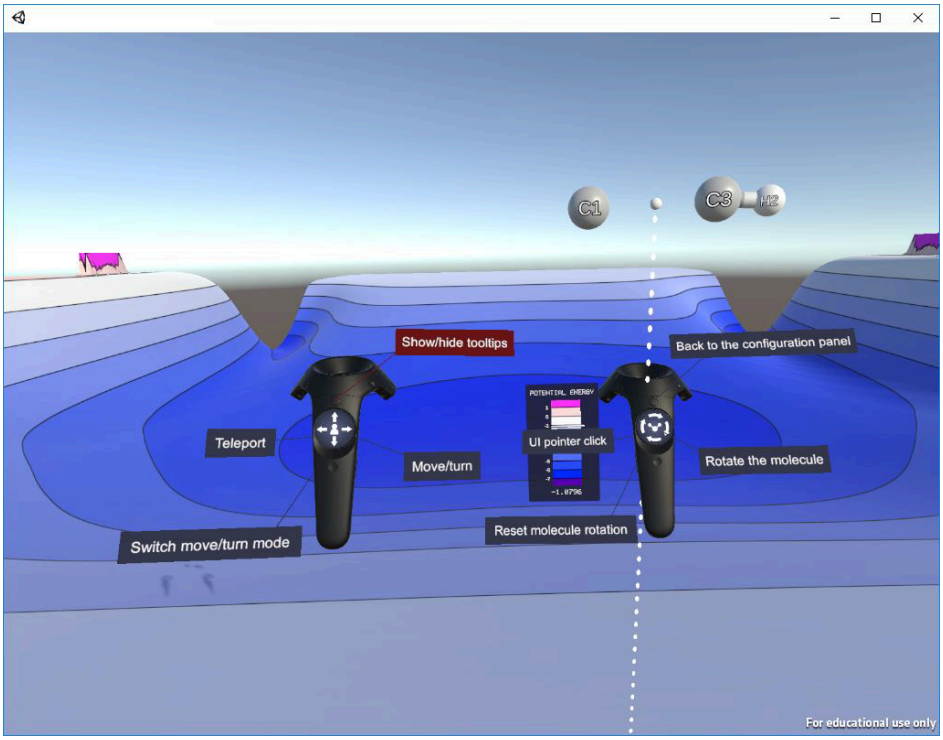

Figure 4: Immersive PES exploration in AVATAR. A set of labels attached to the hand-held controllers informs the user about the available commands.

[2]Shaders are small programs running on the Graphics Processing Unit (GPU). Today's graphics hardware supports several types of specialized shaders, which are used to obtain a vast range of graphical effects and even to perform non-graphics (e.g. scientific) computations.

the color map, with contour lines and intervals. An "unlit"[3] variant of this shader has also been created, mainly for graphical user interface widgets (like the preview map and the color bar of the configuration panel).

With respect to user interaction, we tried to take the best advantage of the handheld controllers of the HTC Vive. Broadly speaking, the left controller is used to navigate across the surface, while the right controller provides information about the current energy value and the associated molecular conformation. As shown in Fig. 4, a set of labels are attached to the controllers, briefly describing the functions performed by each button (and touchpad). The user can toggle the visibility of the labels by pressing the menu button of the left controller.

Although the best way of exploring the energy landscape is by physically moving in the real world, this is only possible for small distances. Therefore, some sort of long-range navigation mechanism is needed. To that purpose, AVATAR provides two common navigation metaphors: "driving" and "teleportation". By touching on the touchpad of the left controller (see Fig. 5 (a)), the user can "slide" over the surface, as if he/she were driving an invisible car. As an alternative, the user can press the trigger button of the left controller to enable the teleportation mode (see Fig. 5 (c)): when the trigger is pressed a ray with a parabolic trajectory and a target at its end appears; the user can then move the controller to choose a destination point and release the trigger to be instantaneously teleported there. Another problem arises when, due to the limited available space in the room, the user is forced to stay in seated position. In these situations, it becomes troublesome to turn the body to look behind (e.g. when the user wants to move towards the opposite side of the surface). As a solution, the user can press the grip button of the left controller to switch from the "driving" to the "turning" mode (and vice versa). Different stickers are drawn over the touchpad to inform the user about the current modality (see Fig. 5 (a) and (b)). When in "turn" mode, it is sufficient to touch the right or the left side of the touchpad to turn the view clockwise or counterclockwise.

A close up view of the right controller is shown in Fig. 6. The information displayed by the controller are related to the point of the surface intersecting the vertical white dotted line.

[3]"Unlit" shaders computes the color of a surface without taking into account lighting information.

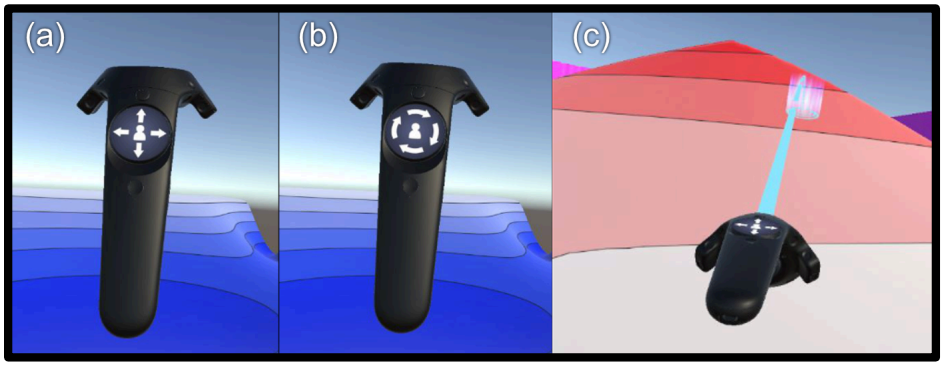

Figure 5: Close up view of the left controller, used for long-range navigation over the PES. By pressing the grip button, the user can switch between "driving" (panel a) and "turning" (panel b) mode. When in driving mode, the user can touch a side of the touchpad to slide over the surface in the corresponding direction. In turning mode, instead, touching the right or the left side of the controller results in turning the view clockwise or counterclockwise. Finally, the user can press the trigger button to enable teleportation (panel c).

Since the energy surface is geometrically described as a set of triangles connected by a shared edge or corner (this is the standard way to describe surfaces in real-time 3D graphics), the information for the considered point are obtained by performing a barycentric interpolation of the data at the vertices of the intersected triangle. The value of the potential energy is shown on a panel attached to the left side of the right controller. A color bar with a moving cursor provides the user with an intuitive estimation of the current energy value, while the actual numerical value is shown on a label placed under the color bar.

As shown in Fig. 6, the molecular system under investigation is kept attached in front of the right controller, centered on its center of mass (indicated by a small white sphere at the beginning of the dotted line). The position of the atoms is updated in real-time as the controller is moved over the PES (note that the molecular system is still displayed in regions of the PES with energy values outside the selected color-map range, while it disappears when entering unphysical regions, i.e. energy values higher than the validity threshold). Although the default orientation of the molecular system is determined by the input atomic coordinates, the user can freely rotate the system by simply touching one of the four sectors (top, bottom, left and right) of the touchpad. This feature is highlighted by a "sticker"

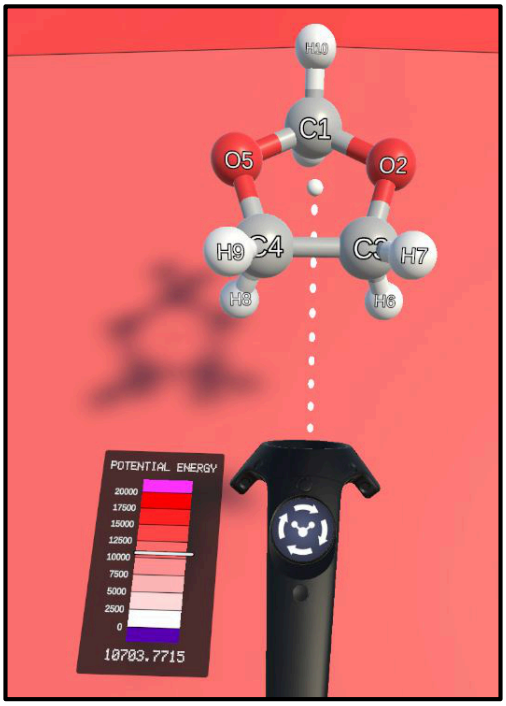

Figure 6: Close up view of the right controller. The sample point is indicated by the intersection of the vertical dotted line with the energy surface. The sampled potential energy is displayed by a color bar widget. The related molecular structure is shown in front of the controller. It is possible to rotate the molecular system by touching on the sides of the touchpad. All the displayed information are updated in real time as the controller is moved over the surface.

drawn over the touchpad (see Fig. 6). The default orientation can be restored at any time by pressing the lateral grip button.

An interesting feature of AVATAR is the ability to visualize bond formation/breaking occurring in chemical reactions, as shown in Fig. 7: when the distance between two atoms is lower than a given threshold, a small cylinder appears to represent the bond formation. Then, as the atoms get closer, the radius of the cylinder increases, up to a maximum value. The reader is referred to Appendix C for further technical details on this aspect.

During the immersive exploration, it is common to want to refine some settings, in order to adjust the size of the PES and/or to improve the color-map range. To this purpose, the user can click on the menu button of the right controller. A dialog box will appear (see Fig.

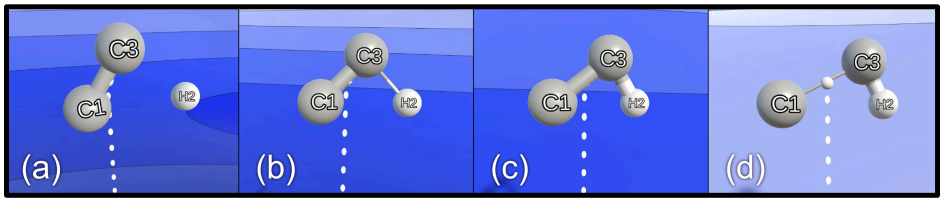

Figure 7: Visual representation of bonds formation and breaking in chemical reactions.

11 in Appendix D) asking the user if he/she really wants to leave the 3D virtual world and return to the configuration panel. To confirm or cancel, it is sufficient to point the controller towards one of the two buttons of the dialog box and press the trigger to click the button. This feature is also used to quit the virtual world once the immersive session is over.

4 Case studies

Competitive reaction paths in $C + CH^+ \rightarrow C_2^+ + H$

As mentioned above, simple reactions of the type A + BC → AB + C are important processes in astrochemistry, especially if the reactants are a netrual-ion or neutral-radical couple and the reaction is barrierless. An important reaction in this class of systems is that of a carbon atom with the methylidyne cation (among the firstly discovered molecules in the diffuse interstellar medium[51], see also Ref. 52), leading to formation of a carbon-carbon bond in C_2^+, a molecule which was detected by mass-spectroscopic sampling in comets Halley[53] and Giacobini–Zinner[54] and which plays a role in ion-molecule reactions leading to production of hydrocarbons in interstellar clouds[55,56].

A PES for the C_2H^+ system has been published and described in Refs. 57 and 58. Here we briefly recall the methodology used to assemble it. The PES was obtained by fitting the well known Aguado–Paniagua[59,60] functional form to a set of 775 three-body and 20 two-body electronic energies obtained by second-order multi-reference perturbation theory (MRPT) in the 'partially contracted' PC-NEVPT2 scheme[61,62]. Configuration-space sampling (ie., the choice of the geometries at which the electronic energies were computed) was performed according to the space-reduced bond-order (SRBO)[63,64] approach allowing for a balanced representation of the attractive and repulsive regions of a diatom configuration space.[65]

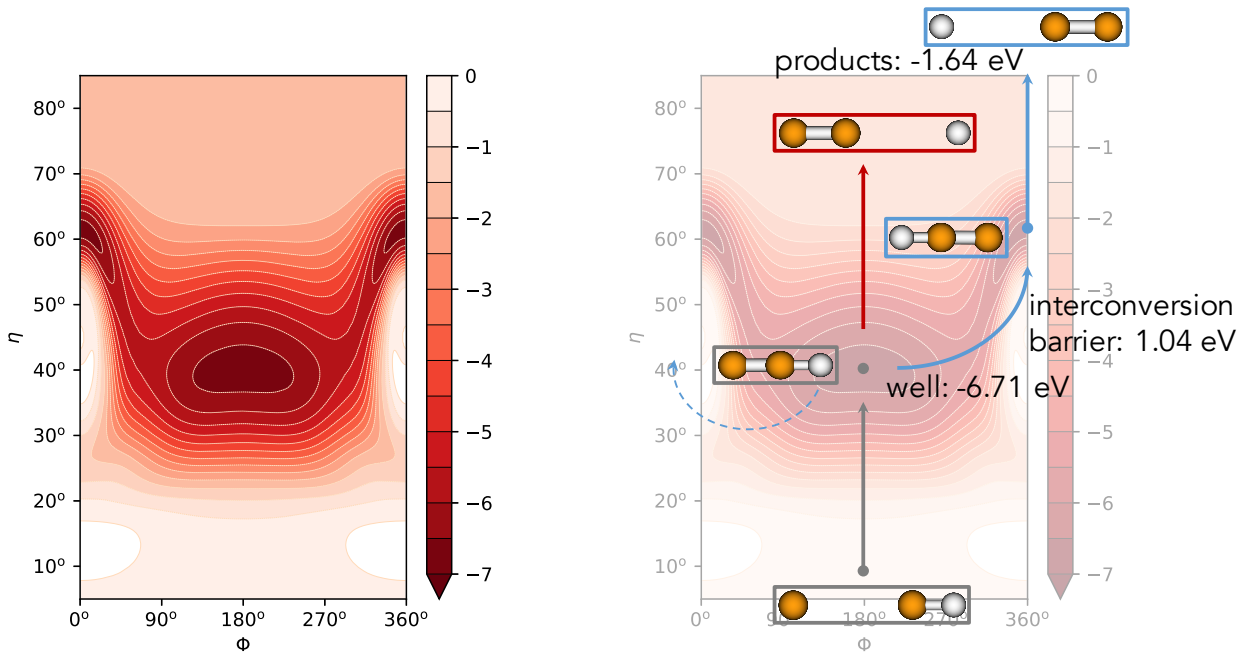

Figure 8: Left-hand side: rectangular relaxed representation of the PES for the C + CH^+ → C_2^+ + H (energy values are in eV). Right-hand side: competing reaction mechanisms superimposed to the PES representation (see Sec. 4 for discussion).

A rectangular relaxed representation of this PES is given in Fig. 8. The energy zero is usually set at the reactants' channel. In a typical IVR session, the user starts in the reactants (C + CH^+) region (bottom edge of the rectangle in Fig. 8) and faces a deep well approximately mid-way on the route to products, which are located at the top edge of the rectangle. Such potential well, as deep as 6.71 eV, corresponds to the barrierless formation of a collinear (the bottom of the well is at $\Phi = 180°$) reaction intermediate C_2H^+ with the C−H bond shorter than the C−C bond ($\eta < 45°$). As the user moves towards the well, he/she will see (floating above the right-hand controller) the C_A atom approaching the C_BH^+ diatom from the carbon side (where labels A and B have been adopted to distinguish between the two carbon atoms), the angle of approach depending on his/her position along the Φ axis. Once the $C_AC_BH^+$ intermediate is reached, the user will realize that, among the infinite alternative paths leading to products, there are two that are more interesting than others. The user can either move on towards products by staying in the middle of the Φ axis (red path in Fig. 8: dissociation into products with the H atom leaving C_2^+ from the C_B side

in a collinear fashion), or explore a second, identical potential well due to rotation of the hydrogen atom about the carbon-carbon bond (blue path in Fig. 8). This last path involves overcoming a mountain pass between the two potential valleys (rotational barrier of 1.04 eV) before forming the linear triatomic $HC_AC_B^+$ and further proceed to products by departure of H from the C_A side. Once in the product region, by looking at the color and at the energy display or simply looking back to the (higher) reactant region, the user will realize that the reaction is exoergic by 1.64 eV

These subtle features of the PES leave their footprints in the dynamics[57] and kinetics[58,66,67] of formation of C_2^+ from C + CH^+, and are of invaluable help in the analysis and interpretation of the outcome of the related calculations. The interested reader is referred to the previously cited works for a more detailed discussion.

Conformational analysis of silacyclopentane

The second example shown in this article is the analysis of the interconversion between conformers in ring-puckering motions of silacyclopentane, a molecule for which experimental far-infrared[68,69], microwave[70] and Raman[71] spectra are available in the literature. A new bidimensional PES for this system has been calculated explicitly for this work. Calculations were performed using the GAUSSIAN16[72] suite of programs with density-functional theory (DFT) by employing B2PLYP as exchange-correlation functional[73] combined with Grimme's D3BJ dispersion[74,75] and maug-cc-pVTZ basis set introduced by Truhlar and coworkers[76,77]. For the sampling of the bidimensional PES a 70×70 uniformly-spaced rectangular grid in $q\cos\theta$ and $q\sin\theta$ was used. The number of calculations to be performed was reduced by exploiting symmetry relations between portions of the circular domain (the energy values in the range $\frac{\pi}{2} < \theta < 2\pi$ are obtained by exploiting the expressions $E(q,\theta) = E(q,\theta+\pi)$ and $E(q,\theta) = E(q,-\theta)$ valid for a 5-term ring whose planar form belongs to C_{2v} symmetry point group).

Each sampled point of the bidimensional PES reported in Figure 9 was calculated independently through a constrained optimization. Each input was constructed using both Cartesian and primitive internal coordinates in the same Z-matrix. Cartesian coordinates in the reference frame defined by Eqs. 6 and 9 of Section 2 have been used in order to specify

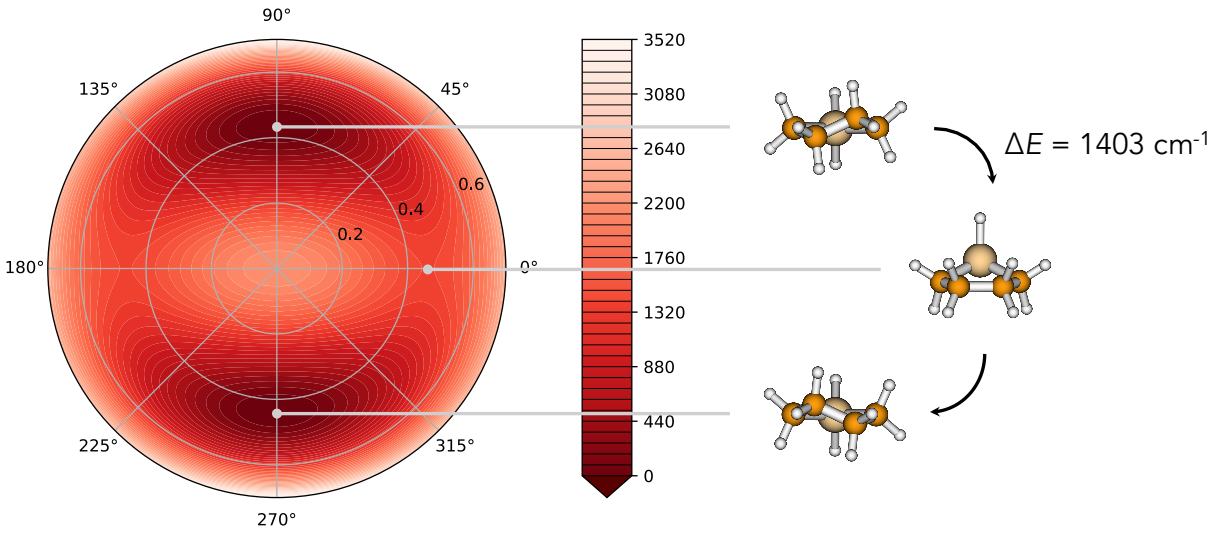

Figure 9: Circular relaxed plot of silacyclopentane as a function of ring-puckering coordinates q and θ (energy values are in cm^{-1}).

the positions of the five atoms involved in the ring structure, while internal coordinates have been used to specify the position of all the other atoms (i.e. all the hydrogen atoms). During the constrained optimization, the z_j Cartesian coordinates of the atoms involved in the ring structure are kept fixed: in this manner the puckering amplitude q and the pseudorotation angle θ are fixed during the optimization. Input files (each one corresponding to a specific couple (q,θ)) have been written automatically with an home-made python script.

In the IVR session with AVATAR, the user starts on the mountain peak at the origin (second-order saddle point), corresponding to the ring planar conformation and being higher in energy of 2193 cm^{-1} with respect to the most stable conformer. This is reached by descending the peak either along the $\Phi = 90°$ line or along the $\Phi = 270°$ line, leading to two symmetric and energetically identical wells corresponding to a twisted structure of C_2 symmetry ($q = 0.436$). These equivalent minima are associated to two enantiomeric structures and are connected by two equivalent transition states of C_s symmetry along a circular path with q comprised between 0.4 and 0.5, and accordingly featuring two mountain passes. Such qualitative description is confirmed by experimental results[68–70].

The barrier to the pseudorotation (the height of the mountain passes above the two potential wells) calculated in this work is 1403 cm^{-1}, which can be compared with the

extrapolations of the barrier obtained from experimental results: the values available in literature are 3.89 Kcal/mol (about 1360 cm^{-1})[68] and 1414 cm^{-1}[71], both in good agreement with the calculated value reported here. The calculated energy of the second-order saddle point associated to the planar conformation of the silacyclopentane ring molecule is 2193 cm^{-1}, to be compared with a lower value of 1559 cm^{-1} already available in literature[71].

5 Conclusions

Arising from the widely adopted Born-Oppenheimer approximation, potential-energy surfaces are central quantities in chemistry. Often reduced to one-dimensional diagrams or sometimes analyzed as two-dimensional contour plots, they offer information on the energetics and mechanisms of chemical processes and represent a useful tool for interpretation of spectroscopic, dynamic and kinetic data.

AVATAR (http://smart.sns.it/avatar) is an IVR application based on modern consumer-grade VR devices specifically designed to exploit our perceptional system for the analysis of bidimensional PESs. The two-stage recipe for PES exploration with AVATAR is to 1) wisely reduce the dimensionality of the PES to two process-tailored, physically meaningful dimensions and to 2) use the associated coordinates as latitude and longitude for representing the energy landscape (energy values as elevation). Whether the two process coordinates are the distances of a breaking and forming bond (such as in S_N2 reactions), two dihedral angles (such as in conformational analysis of proteins), or the more tricky ones presented in this work for an atom-diatom exchange reaction or the analysis of ring-puckering motions, this is up to the user who will have to provide them in a simple multi-model version of the familiar XYZ format.

Immersion in a 3D virtual world by means of consumer-grade head-mounted displays, allows the user to exploit the analogy between the evolution of a chemical process and a pathway through valleys (potential wells) and mountain passes (saddle points) of the associated potential energy landscape for a deeper analysis and interpretation of the PES underlying and governing the chemical process under study. While an additional merit of AVATAR is that it can actually be used for studying any kind of two-dimensional surfaces

(not necessarily those related to the electronic energy of molecular systems), we strongly believe that IVR technology through tools like that presented in this article will significantly impact teaching, training and research in chemistry, and we are currently working at the integration of AVATAR with an ad hoc designed software for modeling the kinetics of multi-well chemical reactions[78].

Acknowledgements

The research leading to these results has received funding from Scuola Normale Superiore through project "DIVE: Development of Immersive approaches for the analysis of chemical bonding through Virtual-reality Environments" (SNS18_B_RAMPINO) and program "Finanziamento a supporto della ricerca di base" (SNS_RB_RAMPINO).

Appendix

A. Input file format

AVATAR requires as input a multi-model "XYZ" file, where each model describes the 3D atomic coordinates associated to a sample point of the energy surface. The energy surface must be sampled according to a regular grid sampling scheme. Each model must specify in its comment line (i.e. the second line of the model) the row and column index of the related sample point within the grid, as well as the associated potential energy. The order of the sample points within the XYZ file is irrelevant.

A schematic description of the input file format is given in Fig. 10.

Where:

- <number of atoms> is the number of atoms in the molecular system. Must be the same for all the models.
- <grid size> is the number of rows and columns composing the grid. Must be expressed in the format: <num rows> x <num columns>

<number of atoms>

G: <grid size> i: <row index> j: <column index> E: <energy value>

<atom 1 symbol> <x coord> <y coord> <z coord>

<atom 2 symbol> <x coord> <y coord> <z coord>

...

<atom n symbol> <x coord> <y coord> <z coord>

<number of atoms>

G: <grid size> i: <row index> j: <column index> E: <energy value>

<atom 1 symbol> <x coord> <y coord> <z coord>

<atom 2 symbol> <x coord> <y coord> <z coord>

...

<atom n symbol> <x coord> <y coord> <z coord>

...

...

...

<number of atoms>

G: <grid size> i: <row index> j: <column index> E: <energy value>

<atom 1 symbol> <x coord> <y coord> <z coord>

<atom 2 symbol> <x coord> <y coord> <z coord>

...

<atom n symbol> <x coord> <y coord> <z coord>

Figure 10: Schematic description of the PES input file for AVATAR.

- <row index> and <column index> are the row and column indices that express the position of the sample point within the grid. Please note that these indices must start from 0.

- <energy value> is the value of the potential energy (energy units are to the users' choice) of the considered sample point. If this field is set to a very high value (with respect to the other values of the PES), the point is considered to not contain valid data (see Appendix B on this). This "trick" can be used to comply with the regular grid sampling scheme constraint when the computed PES has a non-rectangular shape.

- <atom n symbol> is the element symbol of the n-th atom. Each model must contain exactly the same atoms, listed in the same order.

- <x coord>, <y coord> and <z coord> are the coordinates of the atom in the 3D space, expressed in Angstrom.

B. Validity threshold

Since the program supports only a regular-grid sampling scheme, if the pre-computed PES has a non-rectangular shape (such as the circular one discussed in Sec. 4) some special measure have to be taken to "mark" the points of the grid that lies outside the PES. For simplicity, we chose to mark those points by assigning them very high (positive or negative) energy values. That said, the "validity threshold" is an absolute value used by the application to classify the data points: those points having an absolute energy value greater than the threshold are treated as not valid. As an example, consider Fig. 3. Here the computed PES has a triangular shape and the invalid data points are those lying in the pink area outside the triangle. Actually, another pink area can be noticed at the center of the triangle. However, in this case, the pink area represents valid data points whose energy is higher than the upper bound of the color map. In fact, it is advisable to choose the bounds of the color map so as to include only the values we are actually interested in, so as to obtain a more meaningful visual representation of the energy values.

When a dataset is loaded, the application provides default values for the range of the color map and for the validity threshold. These are computed according to the following

procedure:

1. The validity threshold is set to be the 95% of the maximum absolute value in the dataset.

2. The dataset is filtered by ignoring the "invalid" data points in the following steps.

3. Upper and lower fences of the remaining values are computed. These "fences" are metrics widely used in descriptive statistics for identifying the outliers in a dataset. They are defined as follows:

   Upper fence = Q3 + (1.5 * IQR) ; Lower fence = Q1 - (1.5 * IQR)

   where IQR is the interquartile range, while Q1 and Q3 are respectively the first and the third quartile.

4. The values lower than the lower fence or greater than the upper fence are considered outliers and are and ignored in the following steps.

5. Upper and lower fences of the remaining values are computed. They are used as "candidate" range for the color map.

6. The "candidate" range is adjusted so as to obtain human-readable iso-values as well as a proper number of intervals (between 5 and 9). For consistency reasons, the validity threshold is forced to be greater than the maximum absolute value between the bounds of the color map.

Step 6 is also applied to the range of values explicitly set by the user. Finally, it is important to note that all the data points will be displayed in the virtual word, despite of being marked as outliers or "invalid" (with respect to the validity threshold) in the above procedure: they are simply ignored in the computation of the default range for the color map.

C. Visualizing forming and breaking bonds

Another interesting feature of AVATAR is the ability to visualize bond formation/breaking (see Fig. 7): when the distance between two atoms is lower than a given threshold (discussed

later), a small cylinder appears to represent the bond formation. Then, as the atoms gets closer, the radius of the cylinder increases, up to a maximum value.

A common method used by cheminformatics libraries to detect the presence of a covalent bond, is to check if the distance d between two atoms is equal or lower than the sum of their covalent radii r_1 and r_2 plus a tolerance of 0.4 - 0.45 Å (see also Refs. 79,80). We exploited that tolerance to define a "strength" for the bonds:

$$S_{\mathrm{b}} = \begin{cases} 0 & \text{if} \quad d > r_1 + r_2 + 0.5 \\ 1 - 2(d - r_1 - r_2) & \text{if} \quad r_1 + r_2 \leq d \leq r_1 + r_2 + 0.5 \\ 1 & \text{if} \quad d < r_1 + r_2 \end{cases} \tag{13}$$

To provide a graphical representation of bond forming and dissolving it is therefore sufficient to draw a cylinder having a radius equals to the bond strength multiplied by the chosen maximum radius. We chose to adopt a tolerance of 0.5 Å in order to obtain a 20% strength intensity for $d = r_1 + r_2 + 0.4$, so as to visualize a feeble interatomic interaction in the range $r_1 + r_2 + 0.4 < d \leq r_1 + r_2 + 0.5$. One problem we faced was that, due to the discrete nature of the sampled PES, bond information are available only at discrete locations, while we need to approximate bonds strength across the entire energy surface and make it vary in a continuous fashion as the user moves. As already explained, for rendering purposes the program describes the surface as a set of connected triangles. This fact can be exploited when the value of a numerical property for a generic point over the surface is needed: it can be approximated by the weighted average of the values at the vertices of the triangle containing the considered point, using the barycentric coordinates as weights. This approach can also be employed for approximating the bond strength, with the following expedient: if some bonds have been detected only at one or two vertices of the triangle, its strength is considered to be 0 in the remaining vertices.

Spheres and cylinders are drawn using a method known as "GPU-based ray casting of quadric surfaces"[81–83]. This shader-based method, adopted by many modern molecular viewers, allows to visualize a high number of quadric surfaces with a high visual quality, good performance and a greatly reduced amount of data to be transferred to and stored in the GPU. Although it is possible to develop a single shader capable of drawing any quadric surface[82,83], we chose to implement specialized versions for spheres and cylinders in order to

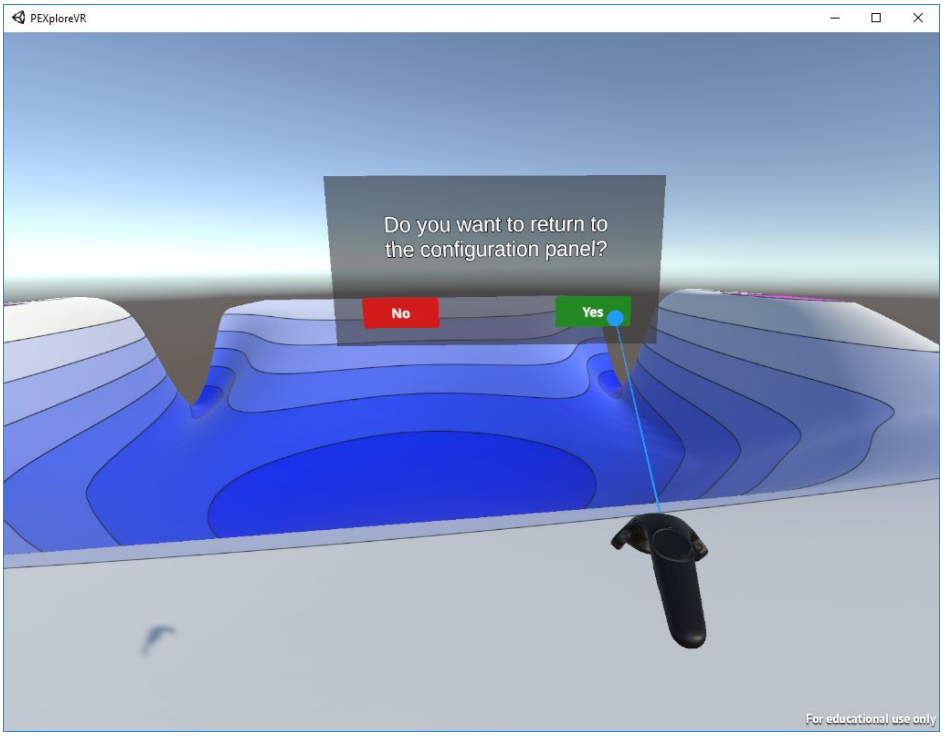

Figure 11: Confirm dialog asking the user if he wants to leave the virtual word and return to the configuration panel. A straight ray starting from the controller is drawn to help the user in pointing the buttons.

maximize the performance.

D. Leaving the virtual world

Once the immersive session is over, by clicking on the menu button of the right controller a dialog will appear asking the user to confirm that he/she wants to leave the 3D virtual world and return to the configuration panel, as shown in Fig. 11. To confirm or cancel, the user has to simply point the controller towards one of the two buttons of the dialog and press the trigger to click the button.

References

1. M. Born and R. Oppenheimer, Ann. Phys. **84**, 457 (1927).

2. V. Barone, M. Biczysko, J. Bloino, M. Borkowska-Panek, I. Carnimeo, and P. Panek, Int. J. Quantum. Chem. **112**, 2185 (2012).

3. V. Barone, M. Biczysko, and J. Bloino, Phys. Chem. Chem. Phys. **16**, 1759 (2014).

4. S. M. Greene, X. Shan, and D. C. Clary, J. Phys. Chem. A **119**, 12015 (2015).

5. S. M. Greene, X. Shan, and D. C. Clary, Adv. Chem. Phys. **163**, 117 (2018).

6. X. Shan, T. A. H. Burd, and D. C. Clary, J. Phys. Chem. A **123**, 4639 (2019).

7. A. Salvadori, M. Fusè, G. Mancini, S. Rampino, and V. Barone, J. Comput. Chem. **39**, 2607 (2018).

8. M. Fusè, I. Rimoldi, E. Cesarotti, S. Rampino, and V. Barone, Phys. Chem. Chem. Phys. **19**, 9028 (2017).

9. G. Bistoni, S. Rampino, F. Tarantelli, and L. Belpassi, J. Chem. Phys. **142**, 084112 (2015).

10. G. Bistoni, S. Rampino, N. Scafuri, G. Ciancaleoni, D. Zuccaccia, L. Belpassi, and F. Tarantelli, Chem. Sci. **7**, 1174 (2016).

11. M. Fusè, I. Rimoldi, G. Facchetti, S. Rampino, and V. Barone, Chem. Commun. **54**, 2397 (2018).

12. M. De Santis, S. Rampino, H. M. Quiney, L. Belpassi, and L. Storchi, J. Chem. Theory Comput. **14**, 1286 (2018).

13. K. H. Marti and M. Reiher, J. Comput. Chem. **30**, 2010 (2009).

14. M. P. Haag, K. H. Marti, and M. Reiher, ChemPhysChem **12**, 3204 (2011).

15. M. P. Haag and M. Reiher, Faraday Discuss. **169**, 89 (2014).

16. S. Amabilino, L. A. Bratholm, S. J. Bennie, A. C. Vaucher, M. Reiher, and D. R. Glowacki, J. Phys. Chem. **123**, 4486 (2019).

17. J. Heer, M. Bostock, and V. Ogievetsky, Commun. ACM **53**, 59 (2010).

18. C. O. S. Sorzano, J. Vargas, and A. P. Montano, arXiv preprint (2014), 1403.2877.

19. A. Altis, P. H. Nguyen, R. Hegger, and G. Stock, J. Chem. Phys. **126**, 244111 (2007).

20. I. Daidone and A. Amadei, Wiley Interdiscip. Rev.: Comput. Mol. Sci. **2**, 762 (2012).

21. L. van der Maaten and G. Hinton, J. Mach. Learn. Res. **9**, 2579 (2008).

22. P. Casavecchia, Rep. Prog. Phys. **63**, 355 (2000).

23. L. Wiesenfeld, W.-F. Thi, P. Caselli, A. Faure, L. Bizzocchi, J. Brandão, D. Duflot, E. Herbst, S. J. Klippenstein, T. Komatsuzaki, et al., arXiv preprint (2016), 1610.00438.

24. S. Rampino, A. Monari, E. Rossi, S. Evangelisti, and A. Laganà, Chem. Phys. **398**, 192 (2012).

25. E. Rossi, S. Evangelisti, A. Laganà, A. Monari, S. Rampino, M. Verdicchio, K. K. Baldridge, G. L. Bendazzoli, S. Borini, R. Cimiraglia, et al., J. Comput. Chem. **35**, 611 (2014).

26. A. Laganà, A. Costantini, O. Gervasi, N. Faginas Lago, C. Manuali, and S. Rampino, J. Grid Comput. **8**, 571 (2010).

27. S. Rampino, N. Faginas Lago, A. Laganà, and F. Huarte-Larrañaga, J. Comput. Chem. **33**, 708 (2012).

28. S. Rampino, D. Skouteris, A. Laganà, and E. Garcia, Lect. Notes Comput. Sci. **5072**, 1081 (2008).

29. A. Laganà, N. Faginas Lago, S. Rampino, F. Huarte Larrañaga, and E. García, Phys. Scr. **78**, 058116 (2008).

30. S. Rampino, D. Skouteris, A. Laganà, E. García, and A. Saracibar, Phys. Chem. Chem. Phys. **11**, 1752 (2009).

31. S. Rampino, D. Skouteris, and A. Laganà, Theor. Chem. Acc. **123**, 249 (2009).

32. S. Rampino, D. Skouteris, and A. Laganà, Int. J. Quantum. Chem. **110**, 358 (2010).

33. A. Laganà and S. Rampino, Lect. Notes Comput. Sci. **8579**, 571 (2014).

34. A. Varandas, Chem. Phys. Lett. **138**, 455 (1987).

35. R. T. Pack and G. A. Parker, J. Chem. Phys. **87**, 3888 (1987).

36. V. Barone, M. Biczysko, J. Bloino, M. Borkowska-Panek, I. Carnimeo, and P. Panek, Int. J. Quantum. Chem. **112**, 2185 (2012).

37. V. Barone, Wiley Interdiscip. Rev.: Comput. Mol. Sci. **6**, 86 (2016).

38. A. Patti, S. Pedotti, G. Mazzeo, G. Longhi, S. Abbate, L. Paoloni, J. Bloino, S. Rampino, and V. Barone, Phys. Chem. Chem. Phys. **21**, 9419 (2019).

39. D. Cremer and J. A. Pople, J. Am. Chem. Soc. **97**, 1354 (1975).

40. L. Paoloni, S. Rampino, and V. Barone, J. Chem. Theory Comput. **15**, 4280 (2019).

41. W. Zou, D. Izotov, and D. Cremer, J. Phys. Chem. A **115**, 8731 (2011).

42. M. Harthcock and J. Laane, J. Mol. Spectrosc. **91**, 300 (1982).

43. R. Meyer, J. Mol. Spectrosc. **76**, 266 (1979).

44. F. Gatti, Y. Justum, M. Menou, A. Nauts, and X. Chapuisat, J. Mol. Spectrosc. **181**, 403 (1997).

45. D. Cremer, J. Phys. Chem. **94**, 5502 (1990).

46. C. Altona and M. Sundaralingam, J. Am. Chem. Soc. **94**, 8205 (1972).

47. A. Wu, D. Cremer, A. A. Auer, and J. Gauss, J. Phys. Chem. A **106**, 657 (2002).

48. D. Cremer, Isr. J. Chem. **20**, 12 (1980).

49. D. Cremer, Isr. J. Chem. **23**, 72 (1983).

50. C. R. Souza, *The Accord.NET Framework*, http://accord-framework.net, (Accessed September 28, 2019).

51. A. E. Douglas and G. Herzberg, Astrophys. J. **94**, 381 (1941).

52. A. T. Myers, C. F. McKee, and P. S. Li, Mon. Not. R. Astron. Soc. **453**, 2747 (2015).

53. D. Krankowsky, P. Lämmerzahl, I. Herrwerth, J. Woweries, P. Eberhardt, U. Dolder, U. Herrmann, W. Schulte, J. J. Berthelier, J. M. Illiano, et al., Nature **321**, 326 (1986).

54. M. A. Coplan, K. W. Ogilvie, M. F. A'Hearn, P. Bochsler, and J. Geiss, J. Geophys. Res.: Space Phys. **92**, 39 (1987).

55. G. Winnewisser, in *Cosmo- and Geochemistry* (Springer Berlin Heidelberg, 1981), vol. 99 of *Top. Curr. Chem.*, pp. 39–71.

56. J. F. Babb, R. T. Smyth, and B. M. McLaughlin, arXiv preprint (2019), `1909.09620`.

57. L. Pacifici, M. Pastore, E. Garcia, A. Laganà, and S. Rampino, J. Phys. Chem. A **120**, 5125 (2016).

58. S. Rampino, M. Pastore, E. Garcia, L. Pacifici, and A. Laganà, Mon. Not. R. Astron. Soc. **460**, 2368 (2016).

59. A. Aguado and M. Paniagua, J. Chem. Phys. **96**, 1265 (1992).

60. A. Aguado, C. Tablero, and M. Paniagua, Comput. Phys. Commun. **108**, 259 (1998).

61. C. Angeli, R. Cimiraglia, and J.-P. Malrieu, J. Chem. Phys. **117**, 9138 (2002).

62. C. Angeli, M. Pastore, and R. Cimiraglia, Theor. Chem. Acc. **117**, 743 (2007).

63. S. Rampino, J. Phys. Chem. A **120**, 4683 (2016).

64. D. Licari, S. Rampino, and V. Barone, Lect. Notes Comput. Sci. **11624**, 388 (2019).

65. S. Rampino and A. Laganà, Int. J. Quantum. Chem. **112**, 1818 (2012).

66. S. C. Althorpe, V. Beniwal, P. G. Bolhuis, J. a. Brandão, D. C. Clary, J. Ellis, W. Fang, D. R. Glowacki, T. J. H. Hele, H. Jónsson, et al., Faraday Discussions **195**, 139 (2016).

67. S. Rampino and Y. V. Suleimanov, J. Phys. Chem. A **120**, 9887 (2016).

68. J. Laane, J. Chem. Phys. **50**, 1946 (1969).

69. J. Durig and J. Willis, J. Mol. Spectrosc. **32**, 320 (1969).

70. J. R. Durig, W. J. Lafferty, and V. F. Kalasinsky, J. Phys. Chem. **80**, 1199 (1976).

71. J. R. Durig, W. J. Natter, and V. F. Kalasinsky, J. Chem. Phys. **67**, 4756 (1977).

72. M. J. Frisch, G. W. Trucks, H. B. Schlegel, G. E. Scuseria, M. A. Robb, J. R. Cheeseman, G. Scalmani, V. Barone, G. A. Petersson, H. Nakatsuji, et al., *Gaussian 16 Revision A.03* (2016), gaussian Inc. Wallingford CT.

73. S. Grimme, J. Chem. Phys. **124**, 034108 (2006).

74. S. Grimme, S. Ehrlich, and L. Goerigk, J. Comput. Chem. **32**, 1456 (2011).

75. L. Goerigk and S. Grimme, J. Chem. Theory Comput. **7**, 291 (2011).

76. E. Papajak, H. R. Leverentz, J. Zheng, and D. G. Truhlar, J. Chem. Theory Comput. **5**, 1197 (2009).

77. E. Papajak and D. G. Truhlar, J. Chem. Theory Comput. **6**, 597 (2010).

78. S. Nandi, D. Calderini, J. Bloino, S. Rampino, and V. Barone, Lect. Notes Comput. Sci. **11624**, 401 (2019).

79. N. M. O'Boyle, M. Banck, C. A. James, C. Morley, T. Vandermeersch, and G. R. Hutchison, Journal of Cheminformatics **3**, 33 (2011).

80. S. Artemova, L. Jaillet, and S. Redon, J. Comput. Chem. **37**, 1191 (2016).

81. S. Gumhold, in *Proceedings of Workshop on Vision, Modelling, and Visualization 2003* (2003), pp. 245–252.

82. R. Toledo and B. Lévy, Tech. Rep., INRIA-ALICE (2004), Extending the graphic pipeline with new GPU-accelerated primitives.

83. C. Sigg, T. Weyrich, M. Botsch, and M. Gross, in *Symposium on Point-Based Graphics*, edited by M. Botsch, B. Chen, M. Pauly, and M. Zwicker (The Eurographics Association, 2006), ISBN 3-905673-32-0, ISSN 1811-7813.